ARTICLE

Electrical Neural Stimulation and Simultaneous *in Vivo* Monitoring with Transparent Graphene Electrode Arrays Implanted in GCaMP6f Mice

Dong-Wook Park,[†,‡,¶] Jared P. Ness,[§,¶] Sarah K. Brodnick,[§] Corinne Esquibel,[§] Joseph Novello,[§] Farid Atry,[#] Dong-Hyun Baek,[§] Hyungsoo Kim,[†] Jihye Bong,[†] Kyle I. Swanson,[⊥,∥] Aaron J. Suminski,[§,⊥] Kevin J. Otto,[□,△,○] Ramin Pashaie,[#] Justin C. Williams,[*,§,⊥] and Zhenqiang Ma[*,†]

[†]Department of Electrical and Computer Engineering, [§]Department of Biomedical Engineering, and [⊥]Department of Neurological Surgery, University of Wisconsin−Madison, Madison, Wisconsin 53706, United States

[‡]School of Electrical and Computer Engineering, University of Seoul, Seoul 130-743, South Korea

[#]Department of Electrical Engineering and Computer Science, University of Wisconsin−Milwaukee, Milwaukee, Wisconsin 53706, United States

[∥]Barrow Neurological Institute, Phoenix, Arizona 85013, United States

[□]J. Crayton Pruitt Family Department of Biomedical Engineering, [△]Department of Neuroscience, and [○]Department of Neurology, University of Florida, Gainesville, Florida 32610, United States

Ⓢ Supporting Information

ABSTRACT: Electrical stimulation using implantable electrodes is widely used to treat various neuronal disorders such as Parkinson's disease and epilepsy and is a widely used research tool in neuroscience studies. However, to date, devices that help better understand the mechanisms of electrical stimulation in neural tissues have been limited to opaque neural electrodes. Imaging spatiotemporal neural responses to electrical stimulation with minimal artifact could allow for various studies that are impossible with existing opaque electrodes. Here, we demonstrate electrical brain stimulation and simultaneous optical monitoring of the underlying neural tissues using carbon-based, fully transparent graphene electrodes implanted in GCaMP6f mice. Fluorescence imaging of neural activity for varying electrical stimulation parameters was conducted with minimal image artifact through transparent graphene electrodes. In addition, full-field imaging of electrical stimulation verified more efficient neural activation with cathode leading stimulation compared to anode leading stimulation. We have characterized the charge density limitation of capacitive four-layer graphene electrodes as $116.07−174.10 \ \mu C/cm^2$ based on electrochemical impedance spectroscopy, cyclic voltammetry, failure bench testing, and *in vivo* testing. This study demonstrates the transparent ability of graphene neural electrodes and provides a method to further increase understanding and potentially improve therapeutic electrical stimulation in the central and peripheral nervous systems.

Electrical stimulation with transparent graphene electrodes

Neural response in GCaMP6f mouse

Graphene vs. Platinum

KEYWORDS: neural electrode, graphene electrode, electrical stimulation, neural implants, GCaMP6
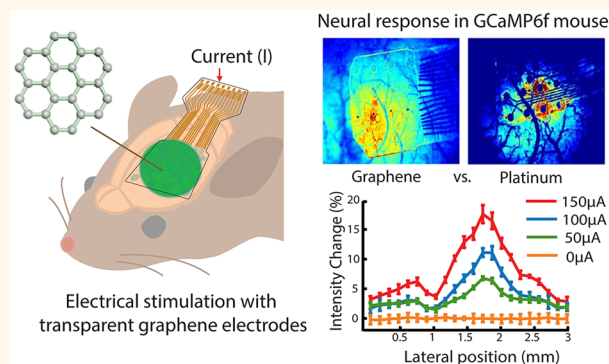
One of the key utilities of implantable neural electrodes is the ability to apply therapeutic electrical stimulation to the central and peripheral nervous systems. Modulation of neural circuits *via* electrical stimulation clinically results in the reduction of motor symptoms such as tremor, rigidity, and slow movement in patients with Parkinson's disease and essential tremor.[1−5] A reduction of seizure frequencies in those suffering from epilepsy has also been reported.[6−9] However, the mechanisms of electrical stimulation in the central and peripheral nervous systems are still poorly understood and need to be
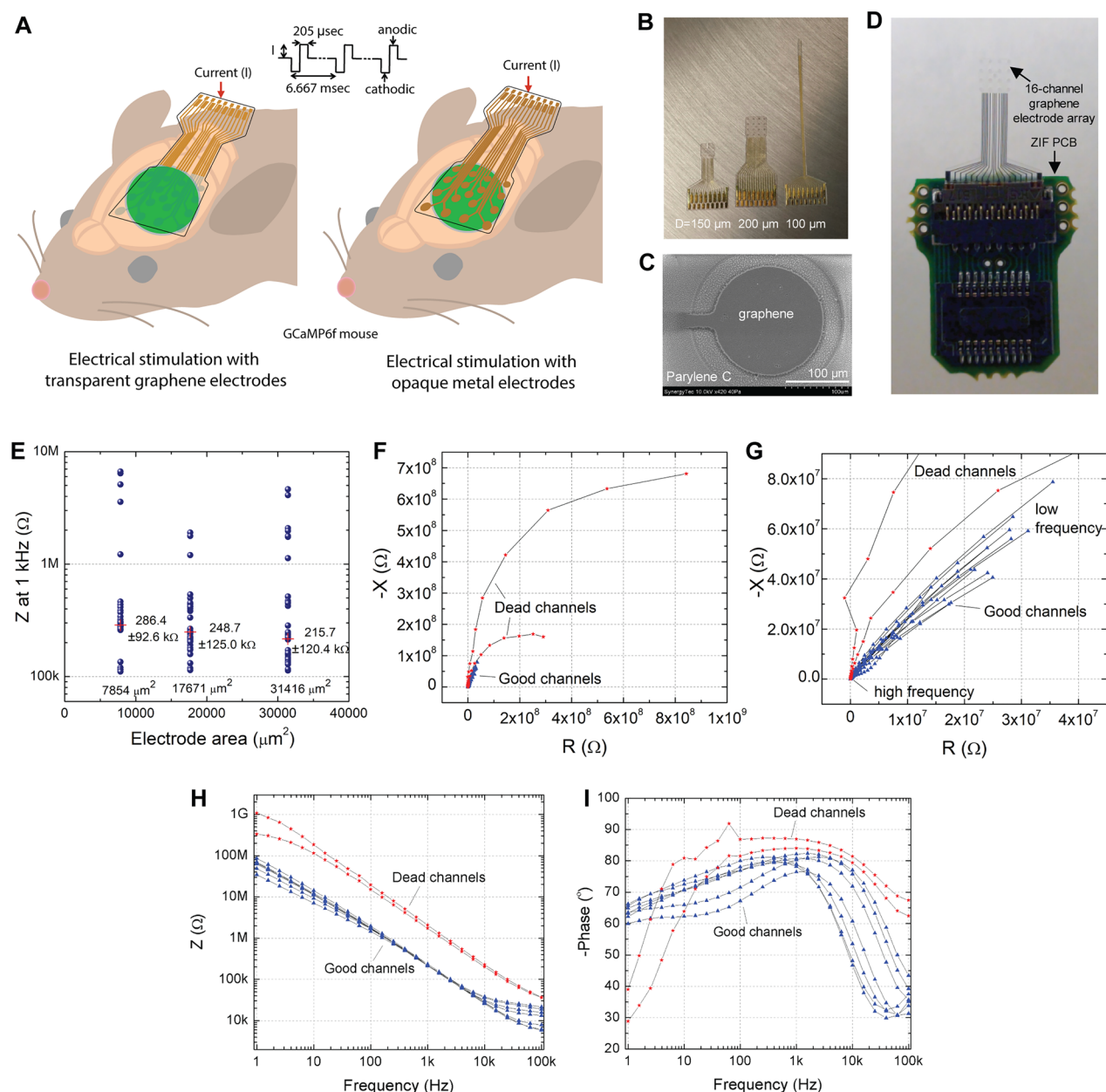
further investigated in order to increase effectiveness and support the application of electrical stimulation as a neuromodulation tool.

Until now, electrical neuromodulation systems have used opaque metal-based neural electrodes (*i.e.*, tungsten (W), platinum (Pt), platinum−iridium (Pt−Ir), and iridium oxide (IrOx)),[10−14] which impede researchers from imaging the

Figure 1. Transparent graphene microelectrocorticography (**µECoG**) electrodes and their electrochemical impedance spectra. (A) Demonstration of microECoG implantation over sensorimotor cortex and electrical stimulation in GCaMP6f mice. Transparent graphene electrodes are beneficial for full-field imaging, whereas opaque metal electrodes hinder direct observation beneath the stimulation electrode. (B) Three different types of graphene multielectrode arrays with varying electrode site diameters (100, 150, 200 μm). (C) SEM image at 420× magnification of a single graphene electrode site (Synergy Technologies LLC, Cedarburg, WI). (D) Graphene microECoG array with 16 transparent electrode sites and a ZIF PCB connector. (E) Impedance (Z) trend for different electrode areas. (F) Nyquist plots of good and dead channels. (G) Magnified view of Nyquist plots. (H) Bode magnitude plots and (I) Bode phase plots of good and dead channels.

activity of neurons and other neural cell types near or beneath the electrode. Opaque electrodes impede optical imaging directly under the electrode site and attached traces (*i.e.*, image artifact). In other words, opaque electrodes block the field of view, resulting in a loss of information during *in vivo* imaging. The development of transparent, carbon-based, graphene neural electrodes could enable a multitude of discoveries that were previously impossible with metal-based opaque neural electrodes, by allowing direct monitoring of the biological scene behind the electrode sites (Figure 1A). The advantages of using transparent graphene electrode arrays over traditional opaque metal-based arrays have been previously demonstrated in

electrophysiology, *in vivo* imaging, and optogenetic experiments.[15−17] Simultaneous neural recordings during optogenetic stimulation in transgenic mice (Thy1-ChR2), standard fluorescence microscopy, and optical coherence tomography (OCT) through graphene-based carbon-layered electrode arrays (CLEAR) were possible due to the wide-spectrum (UV-IR) transparency of graphene electrodes.[15,16] Despite the promising utilities of graphene electrodes, their ability to provide behaviorally relevant electrical stimulation remains unknown. Furthermore, as the supercapacitor property of graphene-based electrodes has been reported for energy storage devices,[18,19] it will be beneficial to characterize the fundamental properties

such as electrochemical impedance spectroscopy (EIS) and cyclic voltammetry (CV) for the graphene neural electrodes.

Here, using EIS, CV, and equivalent circuit modeling, we describe the underlying charge transfer properties of graphene electrodes. The guidelines for charge density limitations through graphene electrodes are provided based on empirical evidence. We also present the spatiotemporal propagation of electrical stimuli in neural tissue using transparent graphene neural electrode arrays implanted in transgenic GCaMP6f mice. *In vivo* fluorescence imaging of neurons with genetically encoded, ultrasensitive calcium indicators (GCaMP6f)[20] enabled the observation of spatiotemporal dynamics of electrical stimulation with minimal image artifact. Monitoring of electrical stimulation over the entire 16-channel electrode array (up to 3.1×3.1 mm^2) was possible due to the highly transparent nature of graphene (*i.e.*, full-field view). Finally, the method was applied to observe the difference in neural activation between two distinct stimulation pulses: cathode leading and anode leading. The discovery of graphene's ability to transfer charge effectively at levels of biological interest has the potential to allow researchers to gain a deeper understanding of the underlying biological mechanisms of electrical stimulation.

RESULTS/DISCUSSION

Fabrication, EIS, and Charge-Carrying Mechanisms of Graphene Neural Electrodes.

Electrochemical impedance spectroscopy is an important tool used to understand the biophysical properties of recording and stimulation electrodes.[21,22] Both the charge density delivered to the subject during electrical stimulation and the electrochemical impedance is dependent on the geometry of the electrode site. To investigate the charge-carrying mechanism of graphene electrodes and the effect of the electrode area on impedance and electrical stimulation, graphene electrodes of different diameters (100, 150, and 200 μm) were fabricated (Figure 1B). The surface areas of these electrodes are 7854, 17 671, and 31 416 μm^2, respectively. Platinum-based electrode arrays were also fabricated to serve as a control. The details of the fabrication process can be found in the experimental section of our previous papers.[15,16] Briefly, transparent graphene electrode arrays with 16 channels were fabricated on a Parylene C substrate. Electrode sites and connecting traces close to the stimulation area are made of patterned four-layer graphene, while the traces far away from the stimulation area and pads are made of stacked titanium (Ti), gold (Au), and platinum (Pt) metals (Figure 1B,C). All of the conductive materials are located on the same Parylene C surface and electrically connected. The four-layer graphene electrode sites and traces are optically clear, having a transmittance of over 90%.[15] Figure 1C shows a scanning electron microscopy (SEM) image at 420× magnification of the graphene electrode site etched from the surrounding polymer substrate. The fabricated electrodes were inserted in a zero insertion force (ZIF) connector on a printed circuit board (PCB) to connect the device to a potentiostat and an electrical stimulator (Figure 1D).

We measured the electrochemical impedance of each electrode at 1 kHz, which is a benchmark frequency of neural electrodes (Figure 1E).[23,24] Channels with an impedance of under 1 MΩ were considered "good", while those with an impedance over 1 MΩ were considered "dead", as high impedance results in noisy electrophysiological recordings of the cerebral cortex (Supplementary Figure 1). The average impedances of good channels were 286.4 ± 92.6, 248.7 ± 125.0, and 215.7 ± 120.4 kΩ for the electrodes with areas 7854 μm^2

($D = 100$ μm), 17 671 μm^2 ($D = 150$ μm), and 31 416 μm^2 ($D = 200$ μm), respectively. As expected, the average impedance decreased as electrode surface area increased, and the majority of good channels ranged between 100 and 600 kΩ at 1 kHz.

Figure 1F–I show representative EIS measurement results of a graphene electrode with a diameter of 200 μm. The Nyquist plot (Figure 1F magnified in 1G) shows that the good channels have lower resistance (R) and reactance ($-X$) compared to dead channels. The Bode plot in Figure 1H depicts the lower impedance (Z) of good channels in the measured frequency range (1–100 kHz). Importantly, the phase of good channels was more than 60° in physiologically relevant frequencies (*i.e.*, 1 to ∼10 kHz), indicating a mainly capacitive charge transfer mechanism (Figure 1I).

Equivalent Circuit Modeling, CV, and Failure Bench Testing.

A graphene electrode was modeled as an equivalent circuit to understand its charge-carrying mechanism (Figure 2A–C). The inset of Figure 2A describes the circuit model composed of four individual elements: a constant phase element impedance (Z_{CPE}), charge transfer resistance (R_{ct}), Warburg impedance (Z_W), and solution resistance (R_s). The Z_{CPE} represents the double-layer capacitance of neural electrodes expressed in eq 1,

$$Z_{CPE} = \frac{1}{Q\omega^n} e^{-(\pi/2)ni} \tag{1}$$

where Q is the magnitude of Z_{CPE}, n is a constant ($0 \leq n \leq 1$), and ω is the angular frequency.

Measurements of electrode properties made in the EIS agreed with the equivalent circuit model (Table 1). The large value of n (0.918) indicates that the graphene electrode's double-layer capacitor is close to that of an ideal capacitor ($n = 1$). Previously, Du *et al.* reported a slightly different phase plot and equivalent circuit for a monolayer graphene electrode introducing an additional constant phase element (C_{PE2}) and leakage resistance (R_L).[25] Although their model could account for the quantum capacitance of graphene, the electrode size in the study was much larger (7 000 000 μm^2) than standard microscale neural electrodes (100–50 000 μm^2).[16,26] Kuzum *et al.* reported the equivalent circuit model for doped graphene.[17] This model used similar equivalent circuit and parameters. The modeling work in these studies shows a capacitive-like charge-carrying mechanism for graphene electrodes, similar to what our results show. Capacitive charge transfer is a desirable property of electrodes used for biological stimulation because of the reduced chemical changes and tissue damage that occur at the tissue–electrode interface, compared to that of the faradaic mechanism of charge transfer.[27] However, note that the impedance of the graphene electrode is 1 or 2 orders higher than that of platinum electrodes (Supplementary Figure 2).

Cyclic voltammetry was used to examine the presence of electrochemical reactions and calculate cathodal charge storage capacity (Q_{cap}) on the surface of graphene electrodes.[21,28] The current–voltage (I–V) characteristics for both good and dead channels are shown in Figure 2D. The good channel ($Z \approx 200$ kΩ) had a peak current of around 50 nA at -0.6 V, while the dead channel ($Z > 1$ MΩ) had a peak current of less than 1 nA, indicating that this channel is not appropriate for electrical stimulation. Furthermore, the peak current range was from 10 to 80 nA at scan rates of 10–1000 mV/s in all good electrodes (Figure 2E). The CV trend of graphene neural electrodes is similar to that of metal-based neural electrodes.[21] Normally, the peak current is proportional to the square root of the scan rate if electron transfer at the electrode surface is limited
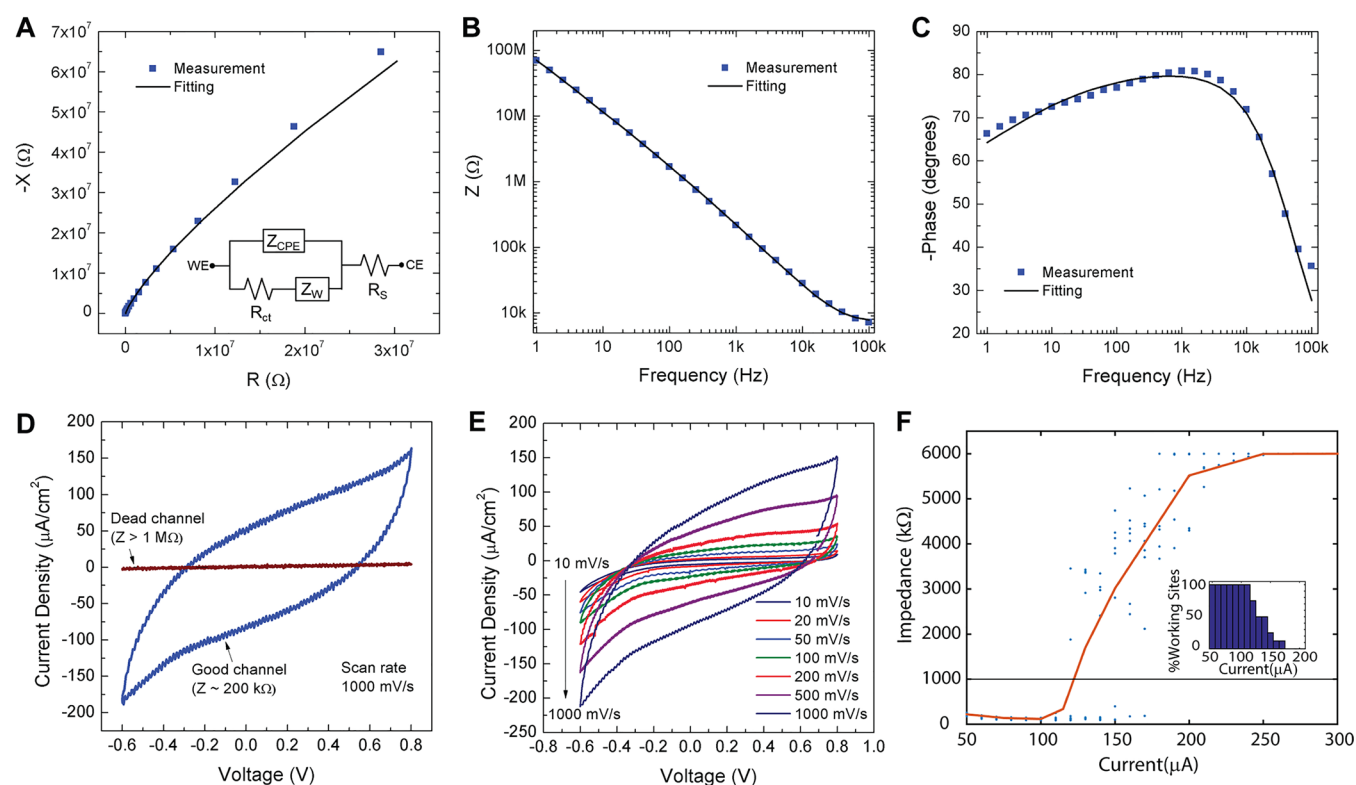
Figure 2. Equivalent circuit modeling, cyclic voltammetry (CV), and failure bench test results of graphene electrodes. (A) Nyquist plot of measurement data and modeling of a graphene electrode with the equivalent circuit (inset). (B) Bode magnitude plot and (C) Bode phase plot with measurement data and equivalent circuit modeling. (D) CV for good ($Z \approx 200$ kΩ) and dead ($Z > 1$MΩ) channels. (E) CV for varying scan rates. (F) Changes in 1 kHz impedance magnitude following electrical stimulation increasing current amplitudes.

Table 1. Parameters of Equivalent Circuit Model

|	Q [S·s^n]	n	R_{ct} [Ω]	R_S [Ω]	Z_W [S·s$^{1/2}$]
graphene (31 416 μm^2) [this work]	1.42×10^{-9}	0.918	1.07×10^{6}	5.92×10^{3}	2.97×10^{-9}
graphene (7 000 000 μm^2) [Du et al.]	5.75×10^{-7} (C_{PE1})	0.673	3.35×10^{3} (R_{ct})	1.71×10^{2}	8.13×10^{-6}
	5.56×10^{-7} (C_{PE2})	0.905	2.34×10^{7} (R_L)		
doped graphene (2500 μm^2) [Kuzum et al.]	5.64×10^{-9}	0.67	84.9×10^{6}		17.36×10^{-9}
platinum (31 416 μm^2) [this work]	1.83×10^{-9}	0.832	1.78×10^{7}	3.36×10^{2}	1.50×10^{-7}

by the diffusion of analyte species.[29] At slow scan rates, the diffusion layer will grow much further from the electrode's surface compared to fast scan rates, leading to lower currents with high capacitance. The Q_{cap} indicates the charge available at the electrode interface, thus helping to evaluate the maximum charge density allowed during electrical stimulation.[21,28] Q_{cap} was calculated by integrating the cathodal (negative) current density enclosed by the CV and dividing by the sweep rate. The calculated Q_{cap} was 87.8 μC/cm^2 for a sweep rate of 1 V/s. The charge-carrying capacity was similar to the experimental charge density values described in the following failure bench testing and *in vivo* electrical stimulation experiments. These CV results not only are helpful to examine the charge-carrying capacity but also can be used to evaluate the viability of the electrodes prior to their use in *in vivo* experiments.

Voltage transients were measured to estimate the safe limit for charge injection into tissue for the graphene electrodes (Supplementary Figure 3A). We estimated charge injection capacity (CIC) using previously published methods[21,30−32] (see Methods section for details) and used a negative polarization potential of −0.6 V as the threshold to determine the maximum CIC. We found the CIC for graphene electrodes to

be 57.13 μC/cm^2, with higher levels of stimulation resulting in negative polarization potentials <−0.6 V (Supplementary Figure 3B).

Lastly, a failure bench test was performed in 0.9% saline solution to estimate the maximum current density that would flow through a graphene electrode site. Electrode impedance (Z) was measured before and after electrical stimulation (205 μs pulse width; 150 Hz; 650 ms total time) on eight graphene electrode sites to examine electrode integrity (Figure 2F). Failure was denoted when a electrode exibited Z above 1 MΩ at 1 kHz. The graphene electrodes with electrical stimulation up to 110 μA had minimal change in Z. Increasing electrical stimulation past this level began displaying failure of the electrode sites, with 50% of the sites failing following stimulation at 130 μA and all failed following stimulation at 180 μA. The average impedance at each electrical stimulaiton value was plotted and fitted to a line. According to the average fit and the 1 M cut off, stimulation past 120 μA (78.3 μC/cm^2) could result in failure of the graphene electrode site. However, note that graphene electrodes in good condition could allow stimulation currents larger than 120 μA.

Electrical Stimulation with Graphene Electrodes *versus* Platinum Electrodes. On the basis of the bench testing evaluation of transparent graphene electrodes, we investigated
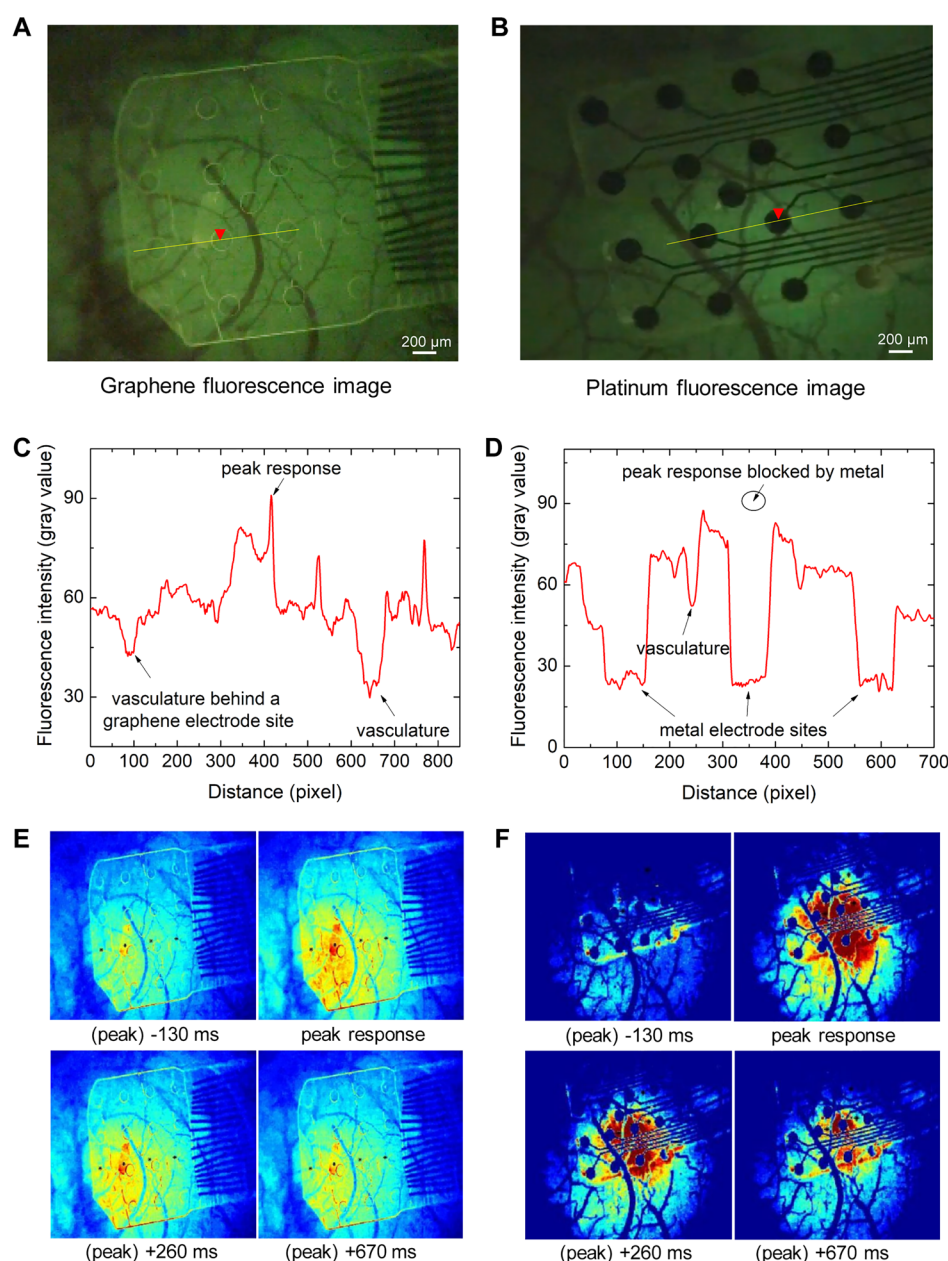
Figure 3. Electrical stimulation delivered to the cortex through a microECoG electrode site and corresponding neural activity *via* fluorescence visualized in GCaMP6f mice. Visualization of the fluorescent neural response after stimulation with (A) a single graphene electrode site (marked with a red triangle) and (B) a single platinum electrode site (marked with a red triangle). (C) Fluorescence intensity over graphene electrodes with minimal artifact (data from yellow dotted line in A). (D) Fluorescence intensity over platinum electrodes with artifact from the electrode sites (data from yellow dotted line in B). (E) Visualization of the intensity of neural response to 100 μA electrical stimulation at times −130 to +670 ms of peak response with the same graphene electrode array as in A. (F) Visualization of the intensity of neural response to 500 μA electrical stimulation at times −130 to +670 ms of peak response with the same platinum electrode array as in B. The 100 μA Pt stimulation result can be found in Supplementary Figure 4.

the capabilities of these electrodes during *in vivo* electrical stimulation using transgenic GCaMP6f mice (two with implanted graphene electrode arrays and one with a platinum electrode array). We have taken advantage of the recently developed genetically modified mouse line incorporating green fluorescent calcium indicator GCaMP6f in subsets of excitatory Thy-1 proteins. GCaMP6f is a fast, highly sensitive, genetically encoded calcium indicator that emits light when the neurons expressing it are activated.[20,33,34] Therefore, it is an excellent model for imaging precise neuronal activity *in vivo*. We have combined our graphene electrode array with chronic *in vivo*

fluorescence imaging of GCaMP6f mice through a cranial window.[16,35] Evoked fluorescence signals were imaged *via* fluorescence microscopy and used to map the spatiotemporal response to electrical stimulation applied through both graphene and platinum (Pt) electrodes.

In this experiment, charge-balanced biphasic current pulses at 150 Hz (205 μs pulse width; 6.667 ms period) were applied for 650 ms through one site on an implanted transparent graphene neural electrode array, and the corresponding fluorescence images were recorded with minimal artifact (Figure 3A). Biphasic stimulation was chosen because it is known to cause less tissue
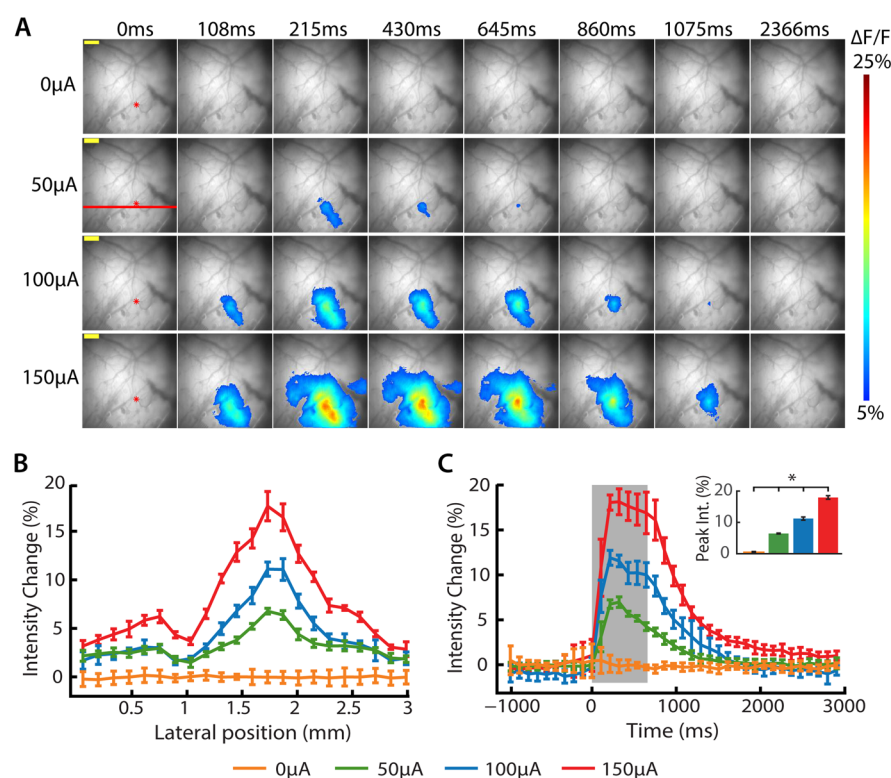
Figure 4. Spatiotemporal responses to varying electrical stimulation currents through a graphene electrode site. (A) Electrical stimulation (50−150 μA; 150 Hz) was applied through a graphene electrode site (red star), and the neural responses were monitored simultaneously. The spatiotemporal responses demonstrate an increased area of neural activation and an increased fluorescence change as applied current increases (scale bar: 500 μm). (B) Spatial response analysis (fluorescence intensity *versus* distance). The maximum fluorescence change was observed from ∼6% (50 μA) to ∼20% (150 μA) at the center of the stimuli. (C) Temporal response analysis (fluorescence intensity change *versus* time). The temporal responses are shown in the horizontal frames presenting the peak responses between 200 and 400 ms after the stimuli. Peak intensity, measured as the average intensity of three frames beginning at 200 ms poststimulation, increased monotonically with increasing stimulation amplitudes (inset). The asterisk indicates a significant difference ($p = 0.05$).

damage compared to monophasic stimulation.[36−38] Fluorescence microscopy demonstrated the potential of graphene electrodes as the fluorescence evoked by neural activity and the cortical vascular system was clearly visible, unlike the Pt-based arrays, which were obstructed (Figure 3A and B). Electrical stimulation at a single electrode site caused widespread depolarization of the cerebral cortex with peak fluorescence (*i.e.*, stimulation evoked neural activity) occurring directly underneath the electrode site. One mouse was used for Figure 3A, C, and E, and a second mouse was used for Figure 3B, D, and F. Figure 3C and D show the fluorescence intensity measured over graphene electrodes and platinum electrodes, respectively. For stable *in vivo* imaging, stimulation currents of 100 and 500 μA were applied through graphene and platinum, respectively. While the 500 μA was the maximum allowed current in our protocol, the current level for graphene was limited to 100 μA based on our bench testing results. Despite the lower stimulation current, graphene electrodes show not only the peak response but also the vasculature beneath electrode sites, which is useful in studying changes in blood flow during electrical stimulation. On the other hand, the peak response and cortical vasculature was largely blocked by platinum electrodes (Figure 3D). Comparison using the same stimulation current (100 μA) can be found in Supplementary Figure 4.

Figure 3E and F show temporal fluorescence images of the cortex with graphene electrodes and platinum electrodes, respectively. It can be clearly seen that the full-field view beneath the graphene electrode sites provides more information than that

of the Pt electrode array, which obscures a partial view of the vasculature and tissues. Movies showing electrical stimulation through the implanted graphene (100 μA) and Pt (100 and 500 μA) electrodes can be found in the Supporting Information (Movies S1, S2, and S3, respectively).

Spatiotemporal Dynamics with Minimal Imaging Artifact. Various levels of electrical stimulation (current = 50, 100, 150, 200, and 300 μA) applied through a graphene electrode site ($D = 150$ μm) were imaged in one mouse using a fluorescence camera (Figure 4A). The corresponding charge densities with current values 50, 100, 150, 200, and 300 μA are 58.03, 116.07, 174.10, 232.13, and 348.20 μC/cm^2, respectively. The current-to-charge-density conversion chart can be found in Supplementary Figure 5. The current amplitude range of 50−300 μA was chosen to verify failure bench test results. Stimulation-induced neural activity was repeatedly viable with currents ranging from 50 to 150 μA in the implanted mouse. Like the bench test results, stimuli at amplitudes greater than 150 μA (200 and 300 μA) increased the probability of electrode failure. Due to this increased failure rate, analysis was restricted to stimulation currents less than or equal to 150 μA. As expected, we observed an increase of neural activation in response to higher stimulation amplitudes. The spatial responses demonstrated an increased area of neural activation and peak response as applied current increased (Figure 4B). Quantitatively, the distance of 5% fluorescence change ($\Delta F/F$) was increased from ∼500 μm (50 μA) to ∼1500 μm (150 μA). The peak neural response (*i.e.*, greatest fluorescence intensity) was observed between
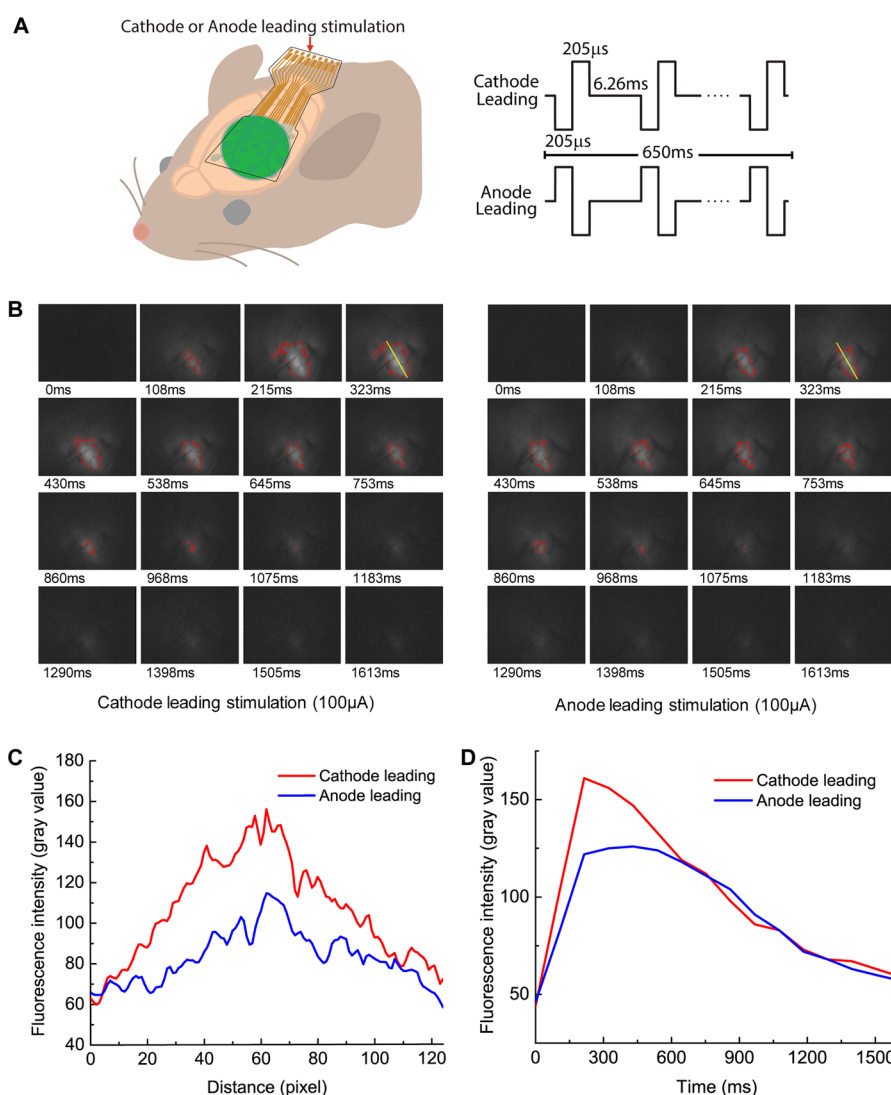
Figure 5. Anode *vs* cathode leading stimulation. (A) Experimental setup and wave schematics of anode and cathode leading stimulation. (B) Spatiotemporal representation of 100 μA electrical stimulation through a graphene electrode site. Cathode leading stimulation shows higher fluorescence intensity as well as faster onset of neural activity. (C) Spatial fluorescence intensity measured at peak response (323 ms). (D) Temporal fluorescence intensity changes. Both spatial and temporal responses show that cathode leading stimulation is more efficient than anode leading stimulation.

200 and 400 ms (Figure 4C) and increased monotonically with increasing stimulation amplitudes. Analysis of variance (ANOVA) found a significant effect of stimulation amplitude ($F_{3,17}$ = 500.1; p = 8.97e^{-17}). *Post hoc t* tests revealed a significant difference in fluorescence intensities between each stimulation level ($p < 0.05$). Importantly, visualization of the spatiotemporal activation dynamics was unimpeded by the electrode sites due to the high transparency of graphene neural electrodes.

These results correspond with the failure bench test results, indicating that graphene neural electrodes will allow a stimulation current up to 100−150 μA (116.07−174.10 μC/cm^2). The different charge density allowance for each electrode may be attributed to the initial condition of the graphene electrode sites, such as the number of defects. In most cases, however, the graphene electrode can stably allow a charge density up to 116.07−174.10 μC/cm^2.

Anode *versus* Cathode Leading Stimulation. Finally, we investigated the effects of cathode leading stimulation (the electrode is driven negative with respect to its prepulse potential) and anode leading stimulation (the electrode is driven positive)

on the neural response in a mouse (Figure 5A). Yazdan-Shahmorad *et al.* reported the difference between the effects of pulse polarity (anodic *vs* cathodic) on the unit firing rate, local field potentials (LFPs), and ECoG signals.[39,40] Their results showed an increase in unit activity following anodic stimulation and a decrease in unit activity following cathodic stimulation in lower layer (V and VI) units. On the other hand, the opposite effect was seen for the units in upper cortical layers (I and II) (*i.e.*, an increase in neural activity following cathode leading stimulation). Manola *et al.* reported a modeling study suggesting that anode leading stimulation preferentially excites neural elements perpendicular to the electrode surface, whereas cathode leading stimulation excites those parallel to its surface.[41] Both studies suggest that the cathode leading stimulation could lead larger and faster neural responses on the brain surface. The electrophysiological monitoring and modeling study can be observed optically with the combination of transparent neural electrodes and GCaMP6f technologies. Here, cathode leading stimulation elicited a stronger neural response (*i.e.*, increased fluorescence) compared to anode leading stimulation (Figure 5B).

Both the spatial response (Figure 5C) and temporal response (Figure 5D) show that the area and peak fluorescence signals were larger in the cathode leading stimulation. This means that more neurons were excited with the cathode leading stimulation. The result corresponds to previous reports in which neurons located in the upper cortical layer have a higher probability of excitation after cathodic stimulation.[39] Also, it can be explained by the different amounts of depolarization occurring during the stimulation; the depolarization with anodic stimulation is roughly one-seventh to one-third that of the depolarization with cathodic stimulation.[42] Our results support the finding that the cathode leading stimulation is more efficient at delivering charge to the brain. However, it should be noted that the neural responses to the different stimulation polarities depend on various neurological conditions. In addition, the stimulation effects are both frequency- and amplitude-dependent.[40] Further studies will be required to fully characterize the effects of polarity on the signal of calcium indicators.

CONCLUSION

In summary, we have demonstrated the viability of electrical stimulation and its simultaneous full-field monitoring with transparent graphene neural electrodes implanted in GCaMP6f mice. The capacitive charge carrying mechanism based on the impedance study of various electrode dimensions suggests that the graphene neural electrode can be a promising neural stimulation tool. Both bench and *in vivo* testing results indicate that the graphene neural electrodes could safely deliver stimulation currents up to $116.07-174.10$ $\mu C/cm^2$. Although this charge density limit is lower than that of other neural electrodes such as Pt ($300-350$ $\mu C/cm^2$)[43,44] and poly(3,4-ethylenedioxythiophene)-poly(styrenesulfonate) (PEDOT−PSS) (3.6 mC/cm^2),[45] it is within the documented limits for safely activating tissue ($10-800$ $\mu C/cm^2$ per phase).[46,47] Therefore, the relatively low charge density limit of graphene would be compatible with most practical *in vivo* electrical stimulation without neural damage. More importantly, the high transparency of the graphene electrode provides experimental advantages that are not available with opaque neural electrodes.

Future work will investigate the relationship between the condition of the graphene electrodes and their charge-carrying capacity and methods for improving the charge density limitation. Regardless, this work demonstrates the utility of graphene electrodes for *in vivo* electrical stimulation and may enable discoveries when combined with other technologies. By using already developed computer models and data analysis techniques, these data may be used to tease apart the various contributors to electrical stimulation effects, such as volume conduction and synaptic propagation. The transparency of the graphene electrodes and traces should extend to other imaging modalities (magnetic resonance imaging, optical coherence tomography, *etc.*). These applications would further validate the use of graphene electrode technology for potential clinical applications. Lastly, the use of this technology with optogenetics as well as different animal disease models will create a multimodal platform for investigating the mechanisms of neuromodulation for various neurological disorders.

METHODS

Device Fabrication. A 4 in. silicon wafer was coated with 15 μm thick Parylene C. The metal traces and pads (Ti/Au = $10/200$ μm) were patterned using photolithography and a lift-off process. The metal traces were not covering the electrode sites where the transparency is needed but only used for interconnection between the ZIF PCB and the electrodes. The four-layer graphene was transferred to the metal patterned substrate, and a silicon dioxide (SiO_2) protection layer was deposited. The graphene/SiO_2 layers were patterned using photolithography to form the electrode sites and part of the traces. A second Parylene C (10 μm) was coated to encapsulate the entire wafer. The first and second Parylene C (25 μm in total) was etched performing photolithography and oxygen (O_2) plasma twice. The outline of the devices was defined in the first and second etching, and the electrode sites and pads were exposed after the second dry etching using the appropriate photomask. The Parylene C was overetched to ensure that no Parylene C residue remained on the electrode surface. Then, the SiO_2 protection layer was etched using 1:6 BOE wet etchant so the graphene surface was exposed to the air. Finally, the fabricated devices were released from the silicon wafer. All three kinds of graphene neural electrodes (D = 100, 150, 200 μm) were designed in the same photomask, so they underwent the same process (Figure 1A). The detailed recipes can be found in our previous papers.[15,16]

Electrochemical Impedance Spectroscopy, Cyclic Voltammetr, and Charge Injection Capacity. A three-electrode system was used with graphene as the working electrode (WE), the platinum as the counter electrode (CE), and Ag/AgCl as the reference electrode (RE) in saline solution. The 16-channel graphene electrode was connected to the Autolab PGSTAT 128N (Metrohm Autolab, The Netherlands) *via* a ZIF PCB. For the EIS, 10 mV sine waves at frequencies from 0.1 to 100 kHz were used, and the parameters of the equivalent circuit were extracted using Nova 1.10 software (Metrohm Autolab). For CV, three cycles of the potential sweep from −0.6 to 0.8 V were applied, and the last cycle curve was plotted to show the stabilized signal. Scan rates ranged from 10 to 1000 mV/sond.

Charge injection capacity of the graphene electrode was measured using previously published methods.[21,30] The same three-electrode system described above was used in these experiments. Charge-balanced, constant-current pulses ($10-80$ μA, cathode leading, 500 μs phases, 100 μs gap between phases) were applied to the WE (return path through the CE). The resulting voltage transient was measured between the WE and RE. The maximum negative polarization potential (E_{mc}) was assumed to be the WE voltage 50 μs following the end of the cathodic phase.

Scanning Electron Microscopy Imaging. SEM images were taken with a backscattered electron detector in low-vacuum (environmental) mode. The pressure was 40 Pa air, and the acceleration voltage was 10 kV. The image (Figure 1C) was acquired at 420× magnification.

Animal Surgery. All animal procedures were approved by the Institutional Animal Care and Use Committee at the University of Wisconsin−Madison. Three C57BL/6J-Tg(Thy1-GCaMP6f)-GP5.5Dkim/J mice (Jackson Laboratories stock number 024276) approximately 6−16 weeks old were used. All experiments were performed during a single terminal imaging session. Animals were pretreated with dexamethasone (2 mg/kg) to prevent cerebral edema, anesthetized with 1−2.5% isoflurane in O_2, and placed on a heat pad, and vital signs were monitored throughout surgery. A bolus injection of 0.25 mL of saline was given subcutaneously for fluid administration. An *in vivo* imaging head holder for mice (SGM-4 Narishige) was used to perform stable surgery and minimize movement artifact for imaging. Once secured, the scalp was removed and a craniotomy was made over the sensorimotor cortex per previously published methods.[16] A 16-channel graphene electrode array was then laid onto the dura with a micromanipulator, and a round glass coverslip was placed over the array and neural tissue. Small pieces of saline-soaked GelFoam were placed along the edges of the glass coverslip to keep the brain moist during the procedure. The ground wire of the electrode array was coiled into a ball and placed into the trapezius muscle in the base of the neck. Approximately 10−15 min before the start of electrical stimulation and fluorescence recording, anesthesia was switched from isoflurane to a ketamine (25−100 mg/kg)/dexmedetomidine (0.05−0.1 mg) cocktail, as isoflurane ablates nearly all cortical signals.

Electrical Stimulation. A 16-channel graphene or platinum electrode array of 150 μm diameter sites was placed on the somatosensory cortex of a GCaMP6f transgenic mouse. The stimulation

return path consisted of a stainless-steel wire placed in the trapezius muscle at the base of the neck. A single site on the electrode was chosen to stimulate the cortex. A pulse train was delivered at 150 Hz with a biphasic pulse duration for 205 μs lasting for 650 ms. The amplitude was varied per trial (50, 100, 150, 200, and 300 μA or respectively 58.03, 116.07, 174.10, 232.13, and 348.20 μC/cm^2) consisting of seven trials. The polarity of the leading pulse was also changed (anode leading *vs* cathode leading) at 100 μA (116.07 μC/cm^2). Pulses were given by AM-Systems Isolated Stimulator Model 2100, which was triggered by the OCT system.

Current to Charge Density Conversion. Charge density applied through an electrode site was calculated using the equation below.

$$\frac{Q_{\text{per phase}}}{A} = \frac{I \times t_{\text{per phase}}}{A}$$

where $Q_{\text{per phase}}$ is the total charge delivered per phase, A is the area of an electrode site, I is the current, and $t_{\text{per phase}}$ is the time for a phase. For instance, 200 μA for 205 μs per phase through a diameter of 150 μm can be calculated as follows.

$$\frac{200 \ (\mu A) \times 0.000205 \ (s)}{0.000176715 \ (cm^2)} = 232.01 \mu C/cm^2/\text{phase}$$

Fluorescence Imaging. The fluorescence images in Figure 3 and Supplementary Movies 1, 2, and 3 were acquired using the light path of a Leica MZ 16F stereoscope in combination with a Sony HDR-SR11 high-definition camcorder. The fluorescence images in Figures 4 and 5 were acquired using a custom-made fluorescence microscope to image an area of 4.6 × 3.4 mm^2 on the brain at a speed of 9.5 frames per second. The microscope employed a GFP filter set, which consisted of an excitation filter (ET470/40x, Chroma), a dichroic beam splitter (FF440/520-Di01, Semrock), and an emission filter (ET525/50m, Chroma). A DG4 illumination system (Sutter Instrument, Novato, CA, USA) served as the excitation light source. The illumination power on the sample was 8 mW over an area of 4 mm in diameter. An objective lens with a magnification of 10× and numerical aperture of 0.1 (LSM02, Thorlabs) was used for illuminating and imaging the sample. The emitted fluorescence light was captured by the objective lens and imaged on a charged coupled device camera (EXi Aqua, QImaging). The length of each imaging sequence was 15 s, which started 4 s prior to the stimulation onset and continued up to 11 s after the onset. The noise of the images was reduced by applying a spatial Gaussian kernel of variance of 3 pixels to the recorded images. Then a baseline image was calculated by averaging all the images that were captured prior to the stimulation onset. The percentile change in the intensity of each pixel with respect to the baseline image was calculated for the poststimulation images and superimposed on the baseline image after color coding.

ASSOCIATED CONTENT

Ⓢ Supporting Information

The Supporting Information is available free of charge on the ACS Publications website at DOI: 10.1021/acsnano.7b04321.

Additional figures (PDF)

Movie S1. Electrical stimulation and monitoring through a graphene electrode array (100 μA) (AVI)

Movie S2. Electrical stimulation and monitoring through a platinum electrode array (100 μA) (AVI)

Movie S3. Electrical stimulation and monitoring through a platinum electrode array (500 μA) (AVI)

AUTHOR INFORMATION

Corresponding Authors

*E-mail (J. C. Williams): jwilliams@engr.wisc.edu.
*E-mail (Z. Ma): mazq@engr.wisc.edu.

ORCID Ⓘ

Dong-Wook Park: 0000-0001-9219-6845

Author Contributions

¶D.-W. Park and J. P. Ness contributed equally to this work.

Author Contributions

D.-W.P., J.P.N., S.K.B., C.E., J.N., F.A., D.-H.B., H.K., J.B., K.I.S., R.P., J.C.W., and Z.M. performed the research. D.-W.P., J.P.N., S.K.B., F.A., K.I.S., A.J.S., K.J.O., J.C.W., and Z.M. wrote the manuscript. D.-W.P., J.P.N., S.K.B., J.C.W., and Z.M. designed the research.

Notes

The authors declare the following competing financial interest(s): D.-W.P, J.C.W., and Z.M. declare competing financial interests in the form of a pending patent application (Transparent and Flexible Neural Electrode Arrays). All other authors declare no competing financial interests.

REFERENCES

(1) Limousin, P.; Krack, P.; Pollak, P.; Benazzouz, A.; Ardouin, C.; Hoffmann, D.; Benabid, A.-L. Electrical Stimulation of the Subthalamic Nucleus in Advanced Parkinson's Disease. *N. Engl. J. Med.* **1998**, *339*, 1105−1111.

(2) Moro, E.; Esselink, R.; Xie, J.; Hommel, M.; Benabid, A.; Pollak, P. The Impact on Parkinson's Disease of Electrical Parameter Settings in Stn Stimulation. *Neurology* **2002**, *59*, 706−713.

(3) Stefani, A.; Lozano, A. M.; Peppe, A.; Stanzione, P.; Galati, S.; Tropepi, D.; Pierantozzi, M.; Brusa, L.; Scarnati, E.; Mazzone, P. Bilateral Deep Brain Stimulation of the Pedunculopontine and Subthalamic Nuclei in Severe Parkinson's Disease. *Brain* **2007**, *130*, 1596−1607.

(4) Benabid, A. L.; Pollak, P.; Hoffmann, D.; Gervason, C.; Hommel, M.; Perret, J.; De Rougemont, J.; Gao, D. Long-Term Suppression of Tremor by Chronic Stimulation of the Ventral Intermediate Thalamic Nucleus. *Lancet* **1991**, *337*, 403−406.

(5) Rehncrona, S.; Johnels, B.; Widner, H.; Törnqvist, A. L.; Hariz, M.; Sydow, O. Long-Term Efficacy of Thalamic Deep Brain Stimulation for Tremor: Double-Blind Assessments. *Mov. Disord.* **2003**, *18*, 163−170.

(6) Racine, R. J. Modification of Seizure Activity by Electrical Stimulation: II. Motor Seizure. *Electroencephalogr. Clin. Neurophysiol.* **1972**, *32*, 281−294.

(7) Berényi, A.; Belluscio, M.; Mao, D.; Buzsáki, G. Closed-Loop Control of Epilepsy by Transcranial Electrical Stimulation. *Science* **2012**, *337*, 735−737.

(8) Kerrigan, J. F.; Litt, B.; Fisher, R. S.; Cranstoun, S.; French, J. A.; Blum, D. E.; Dichter, M.; Shetter, A.; Baltuch, G.; Jaggi, J.; Krone, S.; Brodie, M.; Rise, M.; Graves, N. Electrical Stimulation of the Anterior Nucleus of the Thalamus for the Treatment of Intractable Epilepsy. *Epilepsia* **2004**, *45*, 346−354.

(9) Fisher, R. S.; Velasco, A. L. Electrical Brain Stimulation for Epilepsy. *Nat. Rev. Neurol.* **2014**, *10*, 261−270.

(10) Mayberg, H. S.; Lozano, A. M.; Voon, V.; McNeely, H. E.; Seminowicz, D.; Hamani, C.; Schwalb, J. M.; Kennedy, S. H. Deep Brain

Stimulation for Treatment-Resistant Depression. *Neuron* **2005**, *45*, 651−660.

(11) Shon, Y.-M.; Lee, K. H.; Goerss, S. J.; Kim, I. Y.; Kimble, C.; Van Gompel, J. J.; Bennet, K.; Blaha, C. D.; Chang, S.-Y. High Frequency Stimulation of the Subthalamic Nucleus Evokes Striatal Dopamine Release in a Large Animal Model of Human Dbs Neurosurgery. *Neurosci. Lett.* **2010**, *475*, 136−140.

(12) Hanajima, R.; Dostrovsky, J. O.; Lozano, A. M.; Hutchison, W. D.; Davis, K. D.; Chen, R.; Ashby, P. Somatosensory Evoked Potentials Recorded from Deep Brain Stimulation Electrodes in the Thalamus and Subthalamic Nucleus. *Clin. Neurophysiol.* **2004**, *115*, 424−434.

(13) Johnson, L.; Wander, J.; Sarma, D.; Su, D.; Fetz, E.; Ojemann, J. G. Direct Electrical Stimulation of the Somatosensory Cortex in Humans Using Electrocorticography Electrodes: A Qualitative and Quantitative Report. *J. Neural Eng.* **2013**, *10*, 036021.

(14) Bak, M.; Girvin, J.; Hambrecht, F.; Kufta, C.; Loeb, G.; Schmidt, E. Visual Sensations Produced by Intracortical Microstimulation of the Human Occipital Cortex. *Med. Biol. Eng. Comput.* **1990**, *28*, 257−259.

(15) Park, D.-W.; Schendel, A. A.; Mikael, S.; Brodnick, S. K.; Richner, T. J.; Ness, J. P.; Hayat, M. R.; Atry, F.; Frye, S. T.; Pashaie, R.; Thongpang, S.; Ma, Z.; Williams, J. C. Graphene-Based Carbon-Layered Electrode Array Technology for Neural Imaging and Optogenetic Applications. *Nat. Commun.* **2014**, *5*, 5258.

(16) Park, D.-W.; Brodnick, S. K.; Ness, J. P.; Atry, F.; Krugner-Higby, L.; Sandberg, A.; Mikael, S.; Richner, T. J.; Novello, J.; Kim, H.; Baek, D. H.; Bong, J.; Frye, S. T.; Thongpang, S.; Swanson, K. I.; Lake, W.; Pashaie, R.; Williams, J. C.; Ma, Z. Fabrication and Utility of a Transparent Graphene Neural Electrode Array for Electrophysiology, *In Vivo* Imaging, and Optogenetics. *Nat. Protoc.* **2016**, *11*, 2201−2222.

(17) Kuzum, D.; Takano, H.; Shim, E.; Reed, J. C.; Juul, H.; Richardson, A. G.; de Vries, J.; Bink, H.; Dichter, M. A.; Lucas, T. H.; Coulter, D. A.; Cubukcu, E.; Litt, B. Transparent and Flexible Low Noise Graphene Electrodes for Simultaneous Electrophysiology and Neuro-imaging. *Nat. Commun.* **2014**, *5*, 5259.

(18) Liu, C.; Yu, Z.; Neff, D.; Zhamu, A.; Jang, B. Z. Graphene-Based Supercapacitor with an Ultrahigh Energy Density. *Nano Lett.* **2010**, *10*, 4863−4868.

(19) Wang, Y.; Shi, Z.; Huang, Y.; Ma, Y.; Wang, C.; Chen, M.; Chen, Y. Supercapacitor Devices Based on Graphene Materials. *J. Phys. Chem. C* **2009**, *113*, 13103−13107.

(20) Chen, T.-W.; Wardill, T. J.; Sun, Y.; Pulver, S. R.; Renninger, S. L.; Baohan, A.; Schreiter, E. R.; Kerr, R. A.; Orger, M. B.; Jayaraman, V.; Looger, L. L.; Svoboda, K.; Kim, D. S. Ultrasensitive Fluorescent Proteins for Imaging Neuronal Activity. *Nature* **2013**, *499*, 295−300.

(21) Cogan, S. F. Neural Stimulation and Recording Electrodes. *Annu. Rev. Biomed. Eng.* **2008**, *10*, 275−309.

(22) Chang, B.-Y.; Park, S.-M. Electrochemical Impedance Spectros-copy. *Annu. Rev. Anal. Chem.* **2010**, *3*, 207−229.

(23) Williams, J. C.; Hippensteel, J. A.; Dilgen, J.; Shain, W.; Kipke, D. R. Complex Impedance Spectroscopy for Monitoring Tissue Responses to Inserted Neural Implants. *J. Neural Eng.* **2007**, *4*, 410−423.

(24) Norlin, P.; Kindlundh, M.; Mouroux, A.; Yoshida, K.; Hofmann, U. G. A 32-Site Neural Recording Probe Fabricated by Drie of SOI Substrates. *J. Micromech. Microeng.* **2002**, *12*, 414−419.

(25) Du, X.; Wu, L.; Cheng, J.; Huang, S.; Cai, Q.; Jin, Q.; Zhao, J. Graphene Microelectrode Arrays for Neural Activity Detection. *J. Biol. Phys.* **2015**, *41*, 339−347.

(26) Khodagholy, D.; Gelinas, J. N.; Thesen, T.; Doyle, W.; Devinsky, O.; Malliaras, G. G.; Buzsaki, G. Neurogrid: Recording Action Potentials from the Surface of the Brain. *Nat. Neurosci.* **2015**, *18*, 310−315.

(27) Wang, K.; Fishman, H. A.; Dai, H.; Harris, J. S. Neural Stimulation with a Carbon Nanotube Microelectrode Array. *Nano Lett.* **2006**, *6*, 2043−2048.

(28) Wilks, S. J.; Richardson-Burn, S. M.; Hendricks, J. L.; Martin, D.; Otto, K. J. Poly(3,4-Ethylene Dioxythiophene) as a Micro-Neural Interface Material for Electrostimulation. *Front. Neuroeng.* **2009**, *2*, 7.

(29) Nicholson, R. S.; Shain, I. Theory of Stationary Electrode Polarography. Single Scan and Cyclic Methods Applied to Reversible, Irreversible, and Kinetic Systems. *Anal. Chem.* **1964**, *36*, 706−723.

(30) Wilks, S. J.; Hara, S. A.; Ross, E. K.; Nicolai, E. N.; Pignato, P. A.; Cates, A. W.; Ludwig, K. A. Non-Clinical and Pre-Clinical Testing to Demonstrate Safety of the Barostim Neo Electrode for Activation of Carotid Baroreceptors in Chronic Human Implants. *Front. Neurosci.* **2017**, *11*, 438.

(31) Cogan, S. F.; Troyk, P. R.; Ehrlich, J.; Plante, T. D.; Detlefsen, D. E. Potential-Biased, Asymmetric Waveforms for Charge-Injection with Activated Iridium Oxide Neural Stimulation Electrodes. *IEEE Trans. Biomed. Eng.* **2006**, *53*, 327−332.

(32) Lu, Y.; Lyu, H.; Richardson, A. G.; Lucas, T. H.; Kuzum, D. Flexible Neural Electrode Array Based-on Porous Graphene for Cortical Microstimulation and Sensing. *Sci. Rep.* **2016**, *6*, 33526.

(33) Dana, H.; Chen, T.-W.; Hu, A.; Shields, B. C.; Guo, C.; Looger, L. L.; Kim, D. S.; Svoboda, K. Thy1-Gcamp6 Transgenic Mice for Neuronal Population Imaging. *PLoS One* **2014**, *9*, e108697.

(34) Andrasfalvy, B. K.; Galinanes, G. L.; Huber, D.; Barbic, M.; Macklin, J. J.; Susumu, K.; Delehanty, J. B.; Huston, A. L.; Makara, J. K.; Medintz, I. L. Quantum Dot-Based Multiphoton Fluorescent Pipettes for Targeted Neuronal Electrophysiology. *Nat. Methods* **2014**, *11*, 1237−1241.

(35) Schendel, A. A.; Thongpang, S.; Brodnick, S. K.; Richner, T. J.; Lindevig, B. D.; Krugner-Higby, L.; Williams, J. C. A Cranial Window Imaging Method for Monitoring Vascular Growth around Chronically Implanted Micro-Ecog Devices. *J. Neurosci. Methods* **2013**, *218*, 121−130.

(36) Lilly, J. C.; Hughes, J. R.; Alvord, E. C., Jr; Galkin, T. W. Brief, Noninjurious Electric Waveform for Stimulation of the Brain. *Science* **1955**, *121*, 468−469.

(37) Mortimer, J. T.; Kaufman, D.; Roessmann, U. Intramuscular Electrical Stimulation: Tissue Damage. *Ann. Biomed. Eng.* **1980**, *8*, 235−244.

(38) Mortimer, J. T.; Shealy, C. N.; Wheeler, C. Experimental Nondestructive Electrical Stimulation of the Brain and Spinal Cord. *J. Neurosurg.* **1970**, *32*, 553−559.

(39) Yazdan-Shahmorad, A.; Kipke, D. R.; Lehmkuhle, M. J. Polarity of Cortical Electrical Stimulation Differentially Affects Neuronal Activity of Deep and Superficial Layers of Rat Motor Cortex. *Brain Stimul.* **2011**, *4*, 228−241.

(40) Yazdan-Shahmorad, A.; Kipke, D. R.; Lehmkuhle, M. J. High Gamma Power in Ecog Reflects Cortical Electrical Stimulation Effects on Unit Activity in Layers V/Vi. *J. Neural Eng.* **2013**, *10*, 066002.

(41) Manola, L.; Holsheimer, J.; Veltink, P.; Buitenweg, J. R. Anodal *vs* Cathodal Stimulation of Motor Cortex: A Modeling Study. *Clin. Neurophysiol.* **2007**, *118*, 464−474.

(42) Merrill, D. R.; Bikson, M.; Jefferys, J. G. Electrical Stimulation of Excitable Tissue: Design of Efficacious and Safe Protocols. *J. Neurosci. Methods* **2005**, *141*, 171−198.

(43) Rose, T.; Robblee, L. Electrical Stimulation with Pt Electrodes. VIII. Electrochemically Safe Charge Injection Limits with 0.2 Ms Pulses. *IEEE Trans. Biomed. Eng.* **1990**, *37*, 1118−1120.

(44) Brummer, S.; Turner, M. Electrical Stimulation with Pt Electrodes: II-Estimation of Maximum Surface Redox (Theoretical Non-Gassing) Limits. *IEEE Trans. Biomed. Eng.* **1977**, *5*, 440−443.

(45) Nyberg, T.; Shimada, A.; Torimitsu, K. Ion Conducting Polymer Microelectrodes for Interfacing with Neural Networks. *J. Neurosci. Methods* **2007**, *160*, 16−25.

(46) McCreery, D. B.; Agnew, W. F.; Yuen, T. G.; Bullara, L. Charge Density and Charge Per Phase as Cofactors in Neural Injury Induced by Electrical Stimulation. *IEEE Trans. Biomed. Eng.* **1990**, *37*, 996−1001.

(47) Shannon, R. V. A Model of Safe Levels for Electrical Stimulation. *IEEE Trans. Biomed. Eng.* **1992**, *39*, 424−426.

Supplementary Information

Electrical Neural Stimulation and Simultaneous *In Vivo* Monitoring with Transparent Graphene Electrode Arrays Implanted in GCaMP6f mice

Dong-Wook Park[†, ‡, ¶], Jared P. Ness[§, ¶], Sarah K. Brodnick[§], Corinne Esquibel[§], Joseph Novello[§], Farid Atry[#], Dong-Hyun Baek[§], Hyungsoo Kim[†], Jihye Bong[†], Kyle I Swanson[⊥, //], Aaron J. Suminski[§, ⊥], Kevin J. Otto[□, ■, ○], Ramin Pashaie[#], Justin C. Williams*[§, ⊥], and Zhenqiang Ma*[†]

[†]Department of Electrical and Computer Engineering, [§]Department of Biomedical Engineering, [⊥]Department of Neurological Surgery, University of Wisconsin-Madison, Madison, WI, USA. [‡]School of Electrical and Computer Engineering, University of Seoul, Seoul, South Korea, [#]Department of Electrical Engineering and Computer Science, University of Wisconsin-Milwaukee, Milwaukee, WI, USA. [//]Barrow Neurological Institute, Phoenix, AZ, USA. [□]J. Crayton Pruitt Family Department of Biomedical Engineering, [■]Department of Neuroscience, [○]Department of Neurology, University of Florida, Gainesville, FL, USA.

* Email: mazq@engr.wisc.edu (Z.M.); jwilliams@engr.wisc.edu (J.C.W.)

*[¶]These authors contributed equally to this work.*

KEYWORDS. neural electrode, graphene electrode, electrical stimulation, neural implants, GCaMP6.

Supplementary Figure 1.

Representative electrophysiological recording with good and bad channels.

The evoked neural signals recorded from 16 channels. The signals from bad channels are noisy compared to that from good channels.
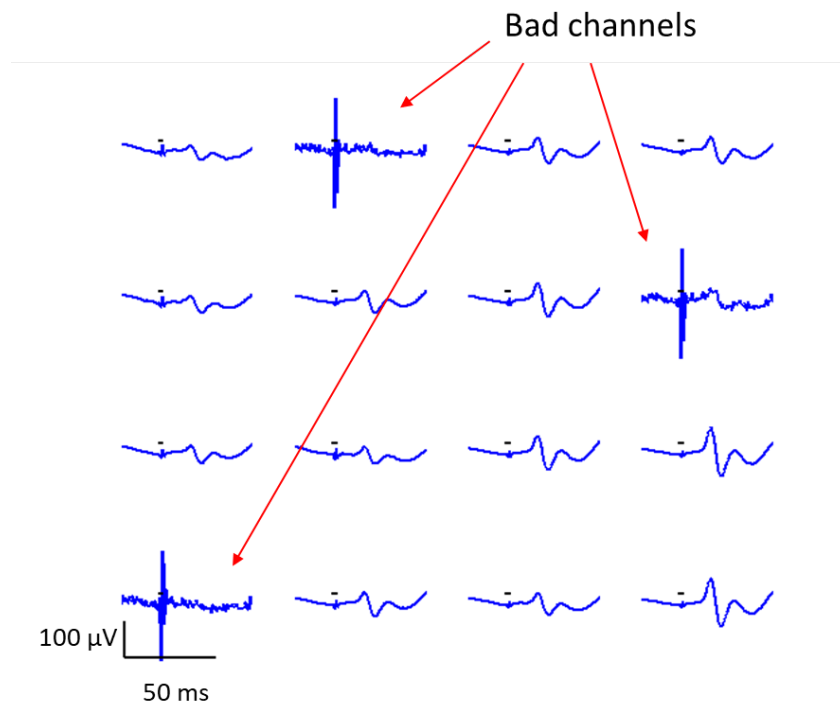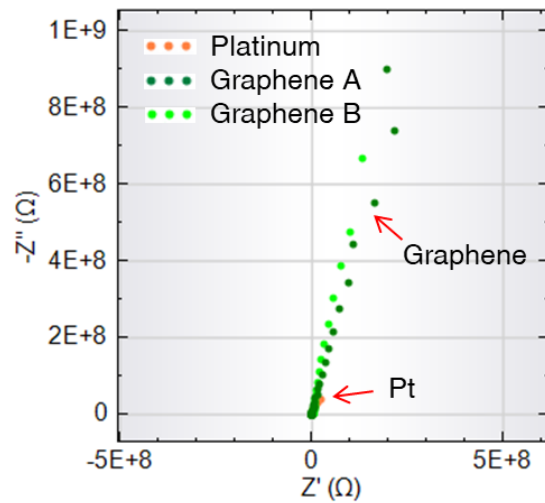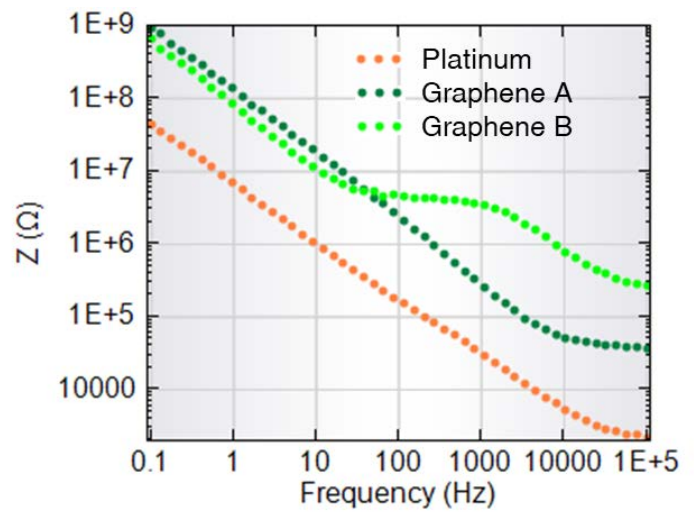
Supplementary Figure 2.

Impedance comparison of graphene and platinum electrodes

(**A**) Nyquist plot and (**B**) Bode magnitude plot of graphene and platinum electrodes. The impedance of graphene is about one or two order higher than that of Pt, which makes the charge density limitation of graphene lower than that of Pt.
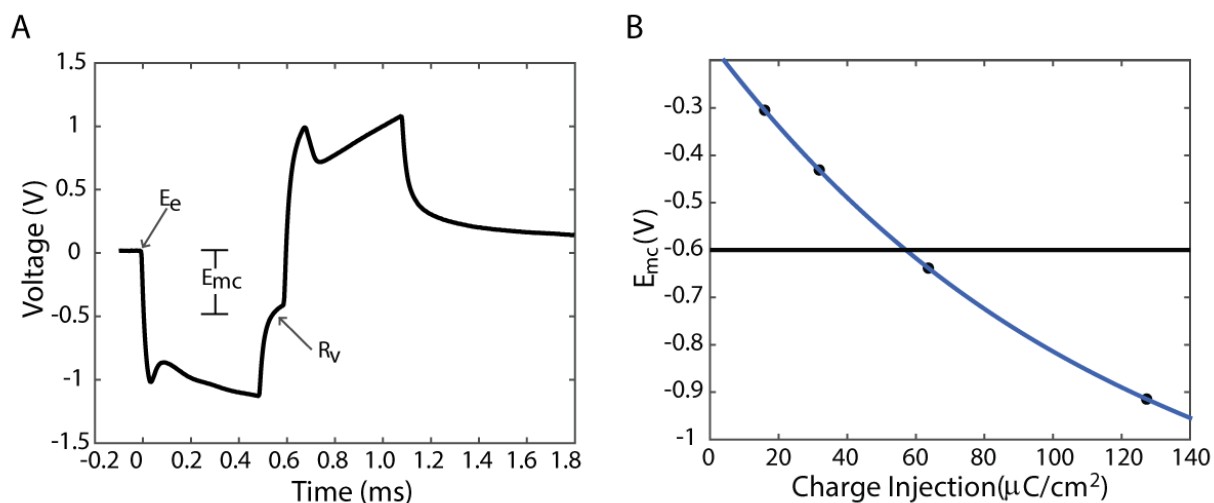
Supplementary Figure 3.

Voltage transients and charge injection capacity (CIC) of graphene electrode

(**A**) Voltage transients and (**B**) Estimated charge injection capacity (CIC) with a negative polarization potential of -0.6V as the threshold. The CIC for graphene electrodes to be 57.13 $\mu C/cm^2$ with higher levels of stimulation resulting in negative polarization potentials < -0.6V. The maximum negative polarization potential (E_{mc}) was assumed to be the WE voltage 50 μs following the end of the cathodic phase.
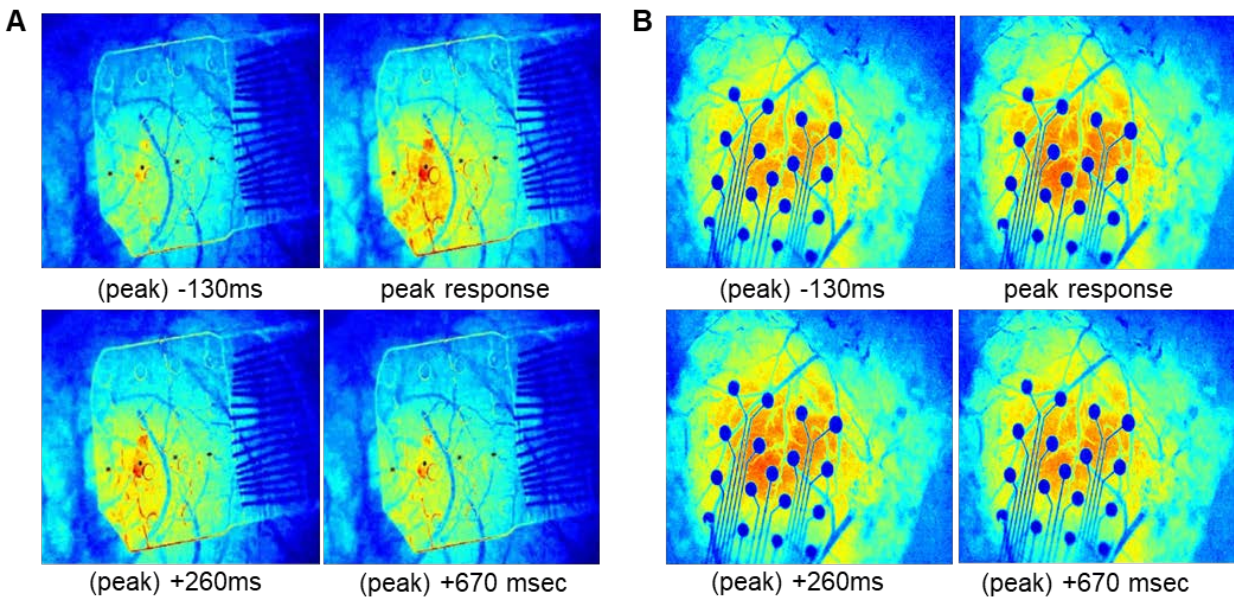
Supplementary Figure 4.

Visualization of neural response to 100 μA electrical stimulation with graphene and platinum electrode.

(**A**) Visualization through graphene electrode and (**B**) platinum electrode. Graphene electrode shows less image artifact due to its transparency.

Supplementary Figure 5.

Current-to-charge density conversion chart for the electrodes with a diameter of 150 µm and 200 µm.

In our *in vivo* experiment, the electrode with D=150 µm was implanted because it was designed to fit brain size of the GCaMP6f mice. However, the device with D=200 µm can be also implantable with a larger craniotomy. The electrode size influences to the charge density (µC/cm²) delivered through the electrode. Hence, the stimulation current should be applied appropriately for different electrode size.

	uC per 205usec phase	Mouse micro-ECoG (150um diameter sites) uC/cm^2 per 205usec phase:	Rat micro-ECoG (200um diameter sites) uC/cm^2 per 205usec phase:
50uA	0.01025	58.03	32.64
100uA	0.0205	116.07	65.29
150uA	0.03075	174.10	97.93
200uA	0.042	232.13	130.57
250uA	0.05125	290.16	163.22
300uA	0.0616	348.20	195.86
350uA	0.07175	406.23	228.50
400uA	0.082	464.26	261.15
450uA	0.09225	522.29	293.79
500uA	0.1025	580.33	326.43